Journal of Materials Chemistry C

Impact of Organic-Inorganic Wavefunction Delocalization on the Electronic and Optical Properties of One-Dimensional Hybrid Perovskites

Journal:	*Journal of Materials Chemistry C*
Manuscript ID	TC-ART-02-2023-000469.R2
Article Type:	Paper
Date Submitted by the Author:	07-Apr-2023
Complete List of Authors:	Ni, Xiaojuan; The University of Arizona, Chemistry and Biochemistry Nanayakkara, Sadisha; The University of Arizona Li, Hong; The University of Arizona, Dept. of Chemistry and Biochemistry Bredas, Jean-Luc ; The University of Arizona, Chemistry and Biochemistry

Impact of Organic-Inorganic Wavefunction Delocalization on the Electronic and Optical Properties of One-Dimensional Hybrid Perovskites

Xiaojuan Ni,† Sadisha Nanayakkara,† Hong Li,* and Jean-Luc Brédas*

Department of Chemistry and Biochemistry, The University of Arizona
Tucson, Arizona 85721-0041, United States

†Equal contributions

Emails: hongli2@arizona.edu
jlbredas@arizona.edu

Abstract

Low-dimensional hybrid organic-inorganic perovskites have attracted a great deal of interest thanks to their high compositional and structural flexibilities that induce distinctive optoelectronic properties, for instance for light-emitting and photovoltaic applications. Here, we study at the density functional theory (DFT) level the electronic and optical properties of two one-dimensional hybrid perovskites incorporating cyanine or Victoria blue B (VBB) dye cations. Our electronic-structure analyses indicate that in both cases the highest occupied molecular orbitals of the cation dyes are nearly aligned with the band edges of the inorganic component; however, wavefunction delocalization between the two components only arises in the cyanine-perovskite system where electronic couplings can be identified, albeit weak, between the organic dye cations and the inorganic framework. The excited-state properties of the cyanine-perovskite system were further evaluated by carrying out time-dependent DFT calculations on representative finite cluster models based on the bulk structures. The electronic couplings between the organic and inorganic components result in a small degree of charge-transfer contributions to the low-lying excited states, which in turn leads to a broadening of the lowest absorption band.

Introduction

Low-dimensional hybrid organic-inorganic perovskites (HOIPs) have received much attention due to their potential for applications as excitonic devices such as solar cells,[1–5] light-emitting diodes,[6–21] photodetectors,[13,22] or lasers.[10,23–26] In comparison to their three-dimensional (3D) counterparts that have rather rigid structural constraints expressed by the Goldschmidt tolerance factor,[27,28] the low-dimensional (1D and 2D) HOIPs allow for a remarkable structural flexibility and offer significantly improved stability. Also, the large tunability of the organic cations incorporated into the perovskite structure provides an extensive compositional space that can be exploited to further improve the structural and optoelectronic properties of these hybrid materials. While most early studies have exploited alkylammonium derivatives as the organic spacers that serve as templating agents and thereby determine the connectivity of the inorganic framework, the incorporation of functional organic cations, such as π-conjugated cations that can directly influence the electronic and optical properties of the HOIPs, has also been studied in a number of recent reports.[29–33]

A particularly interesting feature that remains to be more extensively explored is the possibility with functional organic cations to realize significant electronic couplings between the inorganic components and the organic spacers, which would lead to wavefunction delocalization over both components. Such a characteristic can induce improved charge transport and trigger interesting excitonic behaviors, for instance, the emergence of hybrid excitons or of phosphorescence induced by Dexter-type energy transfer (DET).[31,33–35] The optoelectronic characteristics of HOIPs are influenced by the energy levels of the functional organic cations and inorganic framework at the band edges. This is particularly significant in instances where the electronic states near the Fermi level have a combined contribution, resulting in the delocalization of the wave functions across both components; to the best of our knowledge, such features have not been examined in 1D HOIPs,

where the organic spacers can have larger structural flexibility than in the 3D/2D cases and potentially interact more strongly with the inorganic perovskite (1D) chains.

In recent experimental studies, organic dye cations, such as the heptamethine cyanine Cy7 or Victoria blue B (VBB), have been incorporated with perovskite precursors to form 1D perovskite-like crystalline structures.[36,37] Owing to the near-infrared (NIR) absorbing nature of the dye cations, these hybrid 1D materials have been considered as potential candidates for photovoltaic applications. Also, it is useful to recall that the Cy7 dyes have been used as fluorescence labels and bio-sensors due to their specific NIR photophysical properties;[38–43] by inserting a rigid chlorocyclohexenyl ring within the methine chain, the photostability and fluorescence quantum yield of the dyes are further improved[44,45] (see **Figure 1a)**. On the other hand, the VBB cation dye (see **Figure 1b**)[46,47] is a member of the family of triarylmethane dyes and carries a naphthylamine group.[48]

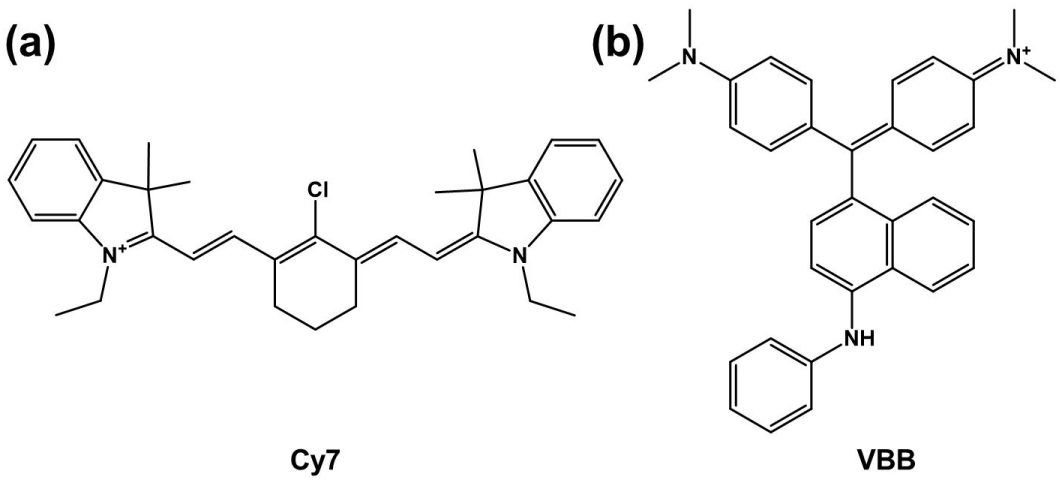

Figure 1. Chemical structures of dye cations considered in this work: (**a**) cyanine (Cy7) and (**b**) Victoria blue B (VBB).

In the present work, to better appreciate the potential of such dye-cation-based 1D perovskites for photovoltaic or light-emitting applications, we investigate their electronic and optical properties with (time-dependent) density functional theory (DFT). In particular, we evaluate the impact of potential electronic couplings between the organic dye cations and inorganic perovskite-like components on these properties, via an analysis of the electronic structures in both the ground state and lowest excited states, which involves a determination of the electronic density of states, band structures, and low-energy excitations.

Methodology

I. 1D perovskites with periodic boundary conditions

The DFT calculations on periodic structures were carried out using the projector-augmented wave method as implemented in the Vienna ab initio simulation package (VASP).[49–51] The geometric structures of the hybrid perovskites were optimized at the Perdew-Burke-Ernzerhof (PBE) level with a Pack-Monkhorst Γ-centered 7 × 3 × 2 k-mesh by relaxing both lattice parameters and atomic coordinates until the total force on each atom was less than 0.01 eV/Å. The plane-wave cutoff energy was set to 500 eV. The range-separated hybrid Heyd-Scuseria-Ernzerhof (HSE) functional incorporating 35% Hartree-Fock exchange was then used with a 3 × 2 × 1 k-mesh to calculate the projected density of states and to evaluate the electronic band structures with consideration of the spin-orbit coupling (SOC) effects.[51,52] The DFT-D3 van der Waals corrections were applied in all calculations.[53] The high-symmetry k-points considered in the band-structure calculations were X (0.5, 0.0, 0.0), Γ (0.0, 0.0, 0.0), Y (0.0, 0.5, 0.0), and Z (0.0, 0.0, 0.5), which were used to define the k-paths with the VASPKIT code.[54]

II. Finite-cluster models simulating the bulk 1D perovskites

Finite-cluster models were exploited to evaluate the excited-state properties of the 1D HOIPs based on Cy7 and VBB. This approach had been adopted in earlier reports investigating the electronic properties of inorganic semiconductors [55–61] as well as 3D and 2D HOIPs.[62–66] Due to the ionic nature of the HOIP materials and the dipolar characteristics of the dye cations, cluster models simulating the bulk HOIPs have to satisfy charge neutrality condition and maintain a minimized dipole moment, a condition imposed by the centrosymmetric crystal structures considered in the present work.

We derived charge-neutral cluster models from the 1D HOIP bulk structures based on their optimized geometries at the DFT/PBE level and carried out single-point DFT and time-dependent DFT (TDDFT) calculations to evaluate the ground-state and excited-state properties. The charge neutrality condition for 1D HOIPs consisting of monovalent organic cations can be described by the following equations:[67-68]

$$\boldsymbol{6n_{pb} = n_{I_1} + 2n_{I_2} + 3n_{I_3}} \quad (1a)$$

$$\boldsymbol{2n_{pb} + n_{MV} = n_{I_1} + n_{I_2} + n_{I_3}} \quad (1b)$$

where the subscript MV stands for monovalent cations and n_{Ii} (i= 1, 2, 3) represents the number of iodine atoms to which each Pb atom in the cluster is bonded. In addition, we note that, due to the charged nature of the dye cations, the total dipole moment of the hybrid clusters cannot be reduced to absolutely zero as in the periodic bulk crystals; thus, we sought to select cluster models that possess the lowest dipole moments.

The Gaussian 16 program[69] was used for all cluster calculations. The excited-state properties were calculated with the long-range corrected ωB97X-D functional,[70] using the 6-31G(d, p) basis set[71] for C, N, H, and Cl atoms, along with the def2SVP[72] effective core potentials for the Pb and I atoms. To simulate the solid-state environment in the cluster calculations, we employed the conductor-like polarizable continuum model[73] with a dielectric constant of $\varepsilon = 36.7$, corresponding to the DMF solvent in which the 1D HOIPs are synthesized, given that residual DMF molecules are present in the crystal structures, see below. A natural transition orbital (NTO) analysis[74] was also performed to better characterize the features that can be related to hybrid excitons. In addition, partition analyses of the charge-transfer (CT) and local-excitation (LE) characteristics for the hole and electron wavefunctions in the excited states were performed to quantify the extent of delocalization over the organic and inorganic components, as implemented in the Multiwfn program.[75]

Results and Discussion

I. Geometric structures

The single-crystal structure of (Cy7)PbI_3·2DMF has been characterized to belong to the P21/c space group, with each unit cell consisting of four Cy7 cations, four $[PbI_3]^-$ octahedra, and eight dimethylformamide (DMF) molecules[36] (see **Figure 2a**). The 1D anionic chains are formed by face-sharing $[PbI_3]^-$ octahedra with Cy7 cations and DMF solvent molecules distributed between them. Each $[PbI_3]^-$ anionic chain is surrounded by four columnar stacks of Cy7 cations, which are aligned nearly parallel to the inorganic chains. The top view in **Figure 2a** illustrates that two adjacent Cy7 cations have either a head-to-head or side-by-side stacking configuration with the

inorganic chains as nearest neighbors. Within each column of Cy7 cations, the distance between the planes of two neighboring polymethine cations is about 3 Å.

(VBB)PbI_3·2DMF is also a 1D HOIP consisting of face-sharing $[PbI_3]^-$ chains with VBB cations and DMF molecules residing in the voids between the inorganic anionic chains[37] (**Figure 2b**). The VBB cations are stacked along the inorganic chains. The DMF solvent molecules act to stabilize the HOIP structure through hydrogen bonds with the primary ammonium moiety of VBB and with short C-H contacts to the $[PbI_3]^-$ chains. The lattice parameters of these two HOIPs, as optimized at the DFT-PBE level, are given in **Table S1** in the Supplementary Information (SI).

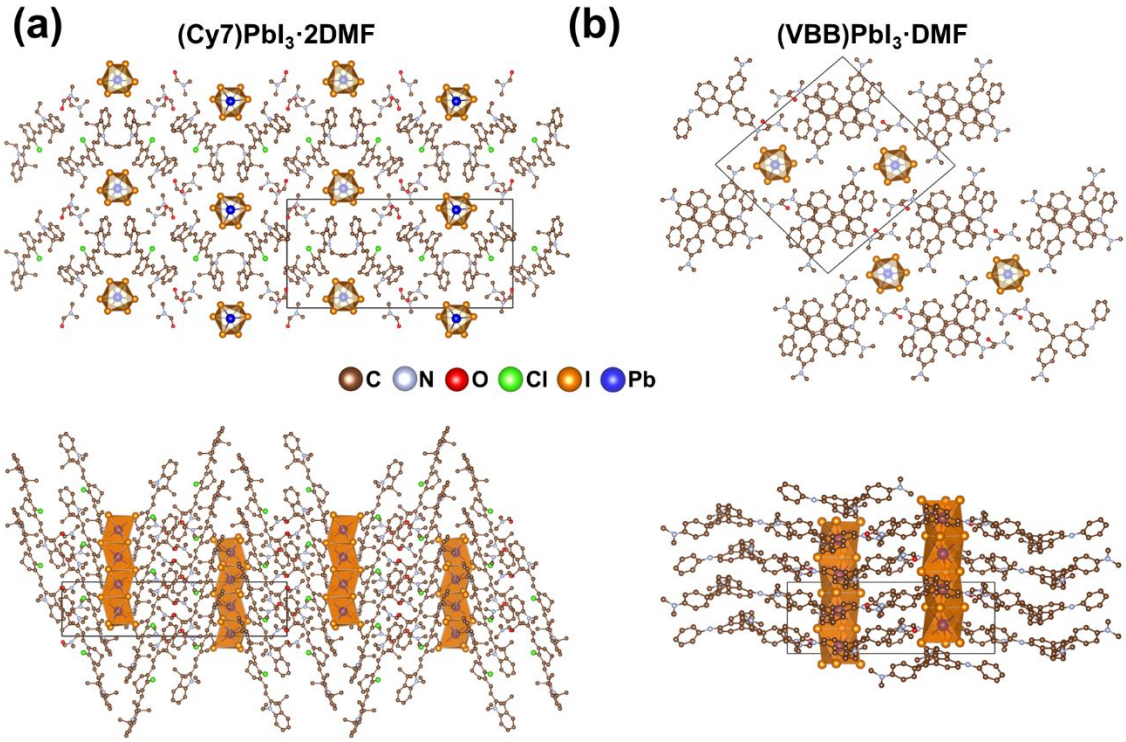

Figure 2. Top view and side view of the crystal structures of (**a**) (Cy7)PbI_3·2DMF and (**b**) (VBB)PbI_3·2DMF. The box indicates the unit cell. Hydrogen atoms are omitted for the sake of clarity.

II. Densities of states and electronic band structures

The projected densities of electronic states in (Cy7)PbI_3·2DMF and (VBB)PbI_3·2DMF were calculated at the HSE+SOC level of theory and are displayed in **Figure 3**. We distinguish the energetic positions of the frontier orbitals originating from the $[PbI_3]^-$ chains and the organic spacers by considering the conduction band minimum (CBM) and valence band maximum (VBM) of the PbI_3-based contributions, and the lowest unoccupied molecular orbital (LUMO) and highest occupied molecular orbital (HOMO) of the organic-cation-based contributions. Our calculations show that the VBM-CBM gaps associated with the $[PbI_3]^-$ 1D chains are 3.69 and 3.93 eV for the Cy7 and VBB HOIPs, respectively; these large values can be attributed to the isolation of the 1D $[PbI_3]^-$ chains by the organic spacers. Importantly, the Cy7/VBB HOMO energies do match the VBM of the $[PbI_3]^-$ 1D fragment, a feature that will be further explored by analyzing the band structures. The small HOMO-LUMO gap of the dye cation then leads to the presence of the Cy7/VBB LUMO level at an energetic position much lower (by about 1.8 eV) than the CBM of the $[PbI_3]^-$ 1D chain; the latter, however, nearly aligns with the LUMO+1 level of the cations.

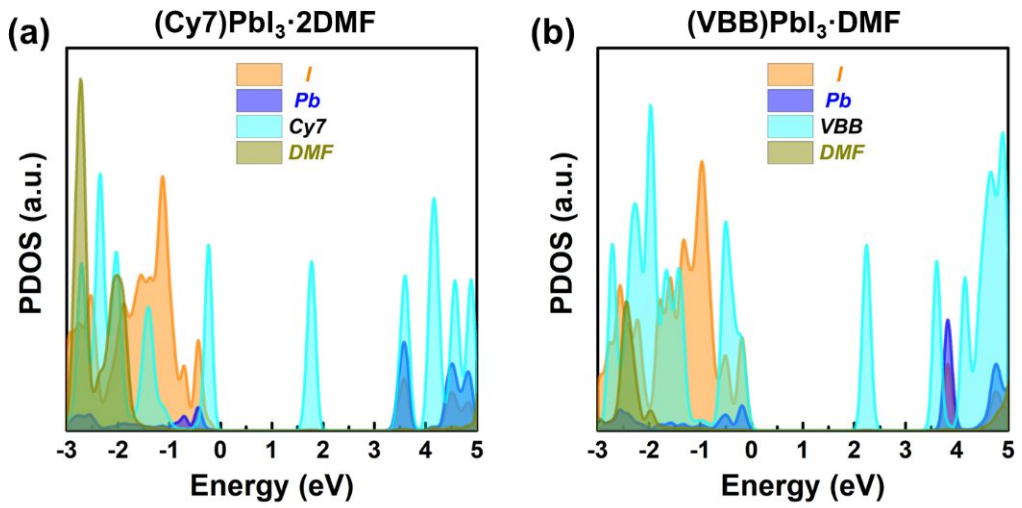

Figure 3. DFT-HSE-SOC projected densities of states for (**a**) (Cy7)PbI_3·2DMF and (**b**) (VBB)PbI_3·2DMF.

To further evaluate the energy-level alignment and electronic hybridization between the organic dyes and inorganic frameworks, we performed band-structure calculations at the HSE+SOC level of theory; the results are depicted in **Figure 4**. In the case of (Cy7)PbI_3·2DMF (see **Figure 4a**), there appear eight nearly degenerate conduction bands at ~1.7 eV above the VBM, which purely derive from the Cy7 LUMO (we recall that there are four Cy7 cations per unit cell, which leads to eight electronic states per molecular level when considering the SOC effect in the calculations). The LUMO+1 level of Cy7 overlaps with the CBM of the inorganic component, with small dispersions observed along the Γ[Y]-X direction (see **Figure 4b**). In the top valence bands of (Cy7)PbI_3·2DMF, the Cy7 nearly degenerate HOMO levels lie right above the VBM of the $[PbI_3]^-$ chains.

Similarly, in (VBB)PbI_3·2DMF, there appear eight nearly degenerate bands within the $[PbI_3]$ VBM-CBM gap, which are related solely to the VBB LUMO level. At the VBM level, see **Figure**

4c, the VBB HOMO energy matches the VBM of the [PbI_3] chain; however, the corresponding partial charge densities (see **Figure S1** in the SI) indicate separate localizations on the organic and inorganic sites without any charge delocalization over the entire framework.

The energy-level alignment between the organic dyes and inorganic [PbI_3] chains in (Cy7)PbI_3·2DMF and (VBB)PbI_3·2DMF is summarized in **Figure 5**.

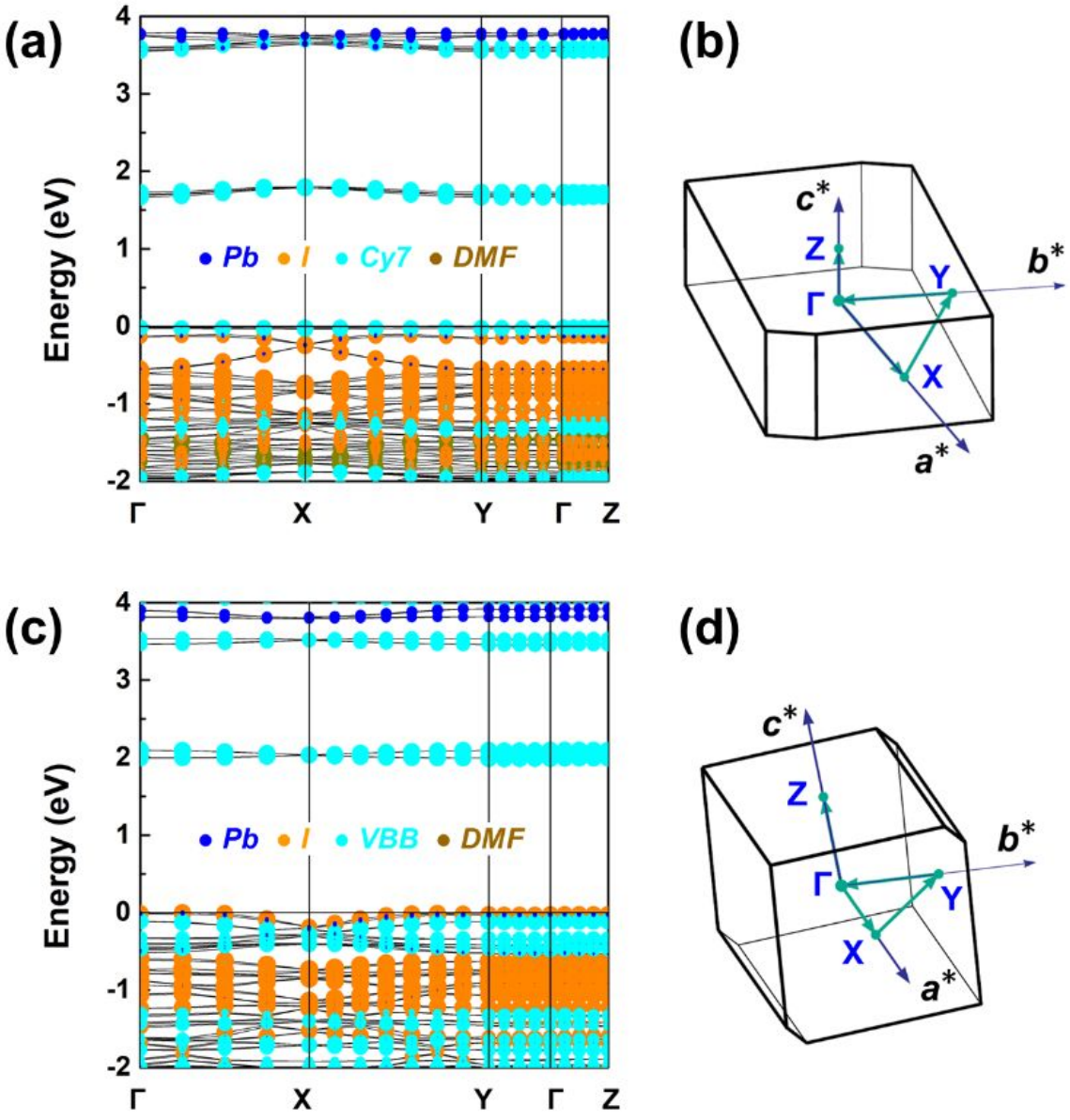

Figure 4. DFT-HSE-SOC band structures and first Brillouin zones of (**a**, **b**) (Cy7)PbI_3·2DMF and (**c**, **d**) (VBB)PbI_3·2DMF. The selected high-symmetry k-paths used to calculate the band structures are highlighted in (**b**) and (**d**). The zero of energy corresponds to the valence band maximum of the hybrid perovskite (with the Fermi level located at the middle of the bandgap).

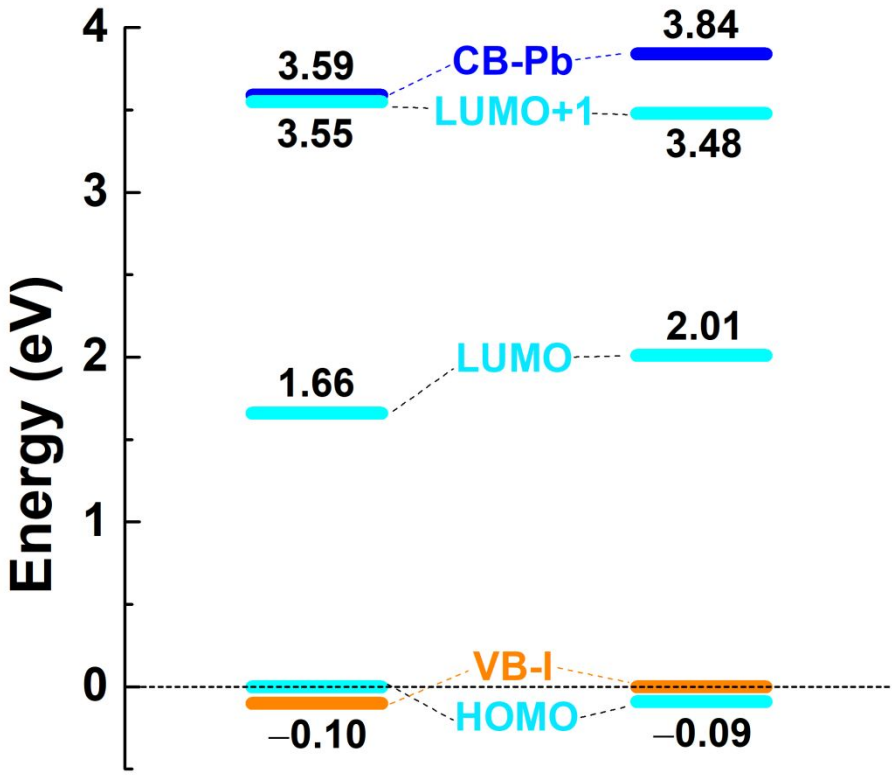

Figure 5. Sketch of the DFT-HSE-SOC energy-level alignments between the dye cations and perovskite layers in (Cy7)PbI_3·2DMF and (VBB)PbI_3·2DMF. The dye cation MO levels and perovskite Pb and I frontier levels are color-coded in cyan, blue, and orange, respectively. All energy values are given in eV, with the VBM of the hybrid perovskites taken as the zero of energy.

III. Electronic hybridization and coupling strength between Cy7 and [PbI_3] in (Cy7)PbI_3·2DMF

Zooming into the energy windows of interest for (Cy7)PbI_3·2DMF, as depicted in **Figure 6**, shows the presence of the sought-after electronic hybridization between the Cy7 LUMO+1 level and the CBM of the [PbI_3] chains as well as between the Cy7 HOMO level and the VBM of the [PbI_3] chains. The real-space partial charge density distributions of those electronic states (marked by the red boxes in the left panels of **Figure 6**) indicate that the Cy7 LUMO+1 and HOMO levels are indeed electronically coupled with the [PbI_3] chains, as illustrated in the right panels of **Figure 6**.

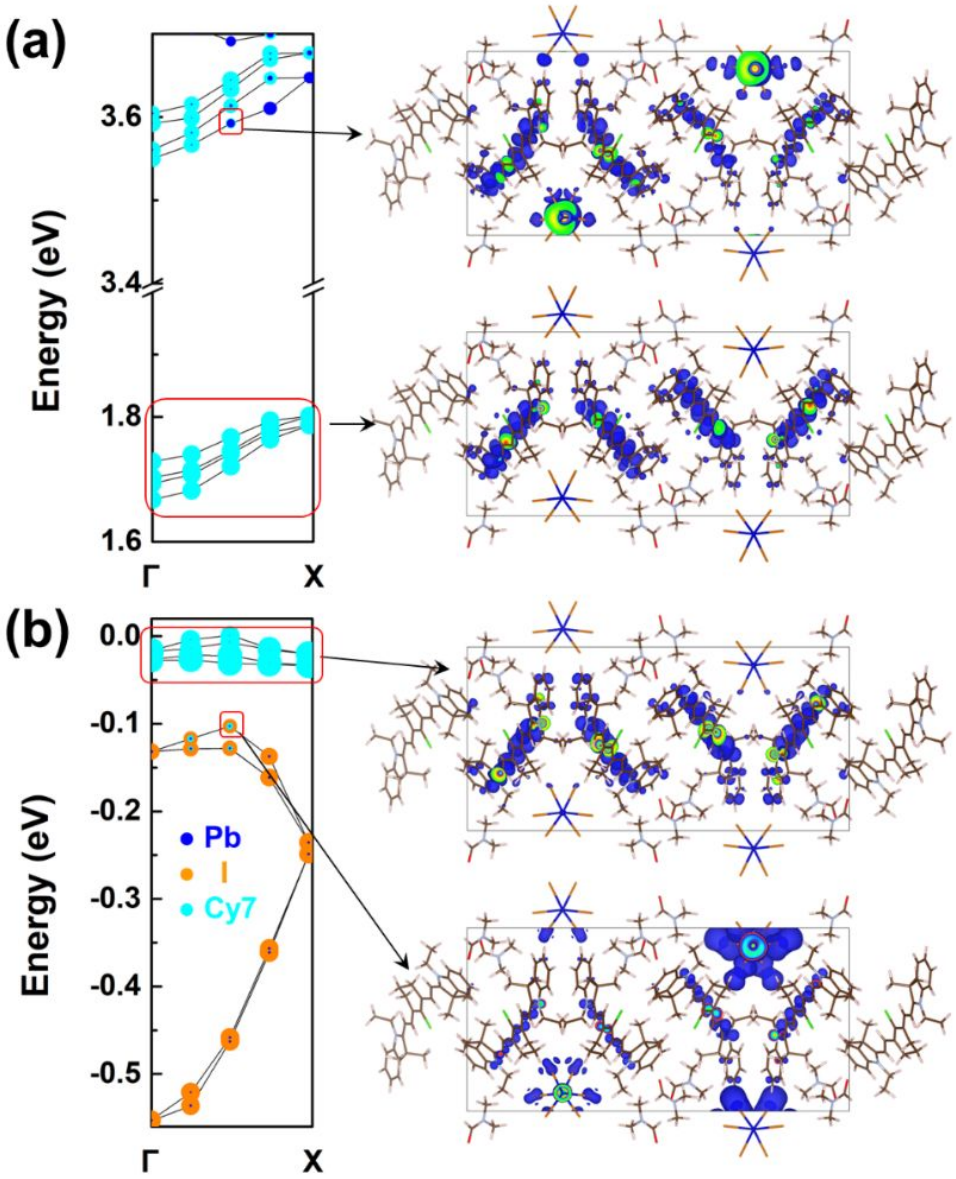

Figure 6. (Cy7)PbI_3·2DMF: DFT-HSE-SOC band structures along the Γ-X k-path and partial charge densities of the electronic states indicated by the red boxes: (**a**) conduction bands and (**b**) valence bands.

To further evaluate the electronic coupling strength between the organic and inorganic components in (Cy7)PbI_3·2DMF, we turned to tight-binding (TB) model analyses to quantitatively describe the top valence bands in (Cy7)PbI_3·2DMF. The lattice model is illustrated in **Figure 7a**. Detailed

descriptions of the TB models are provided in the SI. The band structure obtained from our TB model (see **Figure 7b**) reproduces very well the DFT-HSE calculated bands (see **Figure 7c**) when using a coupling strength parameter between the Cy7 HOMO level and PbI3 chains of ~39 meV; this value is comparable to that we previously reported for an anthracene-based (2,2'-(anthracene-2,6-diyl)bis(ethan-1-ammonium) (AnBE)) 2D perovskite, $AnBEPbI_4$.[33] By varying the coupling strength between Cy7 and $[PbI_3]$ as well as the $[PbI_3]$ on-site energy (see **Figure S2** in the SI), both the interaction between Cy7 and $[PbI_3]$ and the relative on-site energy levels are found to be responsible for the hybridization between the organic and inorganic components in the HOIP. These results further point out that, by changing the on-site energy of the inorganic chain via the consideration of a different divalent metallic atom (*e.g.*, Sn) and/or a different halogen (Cl or Br), the energy-level alignment and organic-inorganic electronic couplings in the 1D HOIPs could be further tuned and provide another degree of versatility.

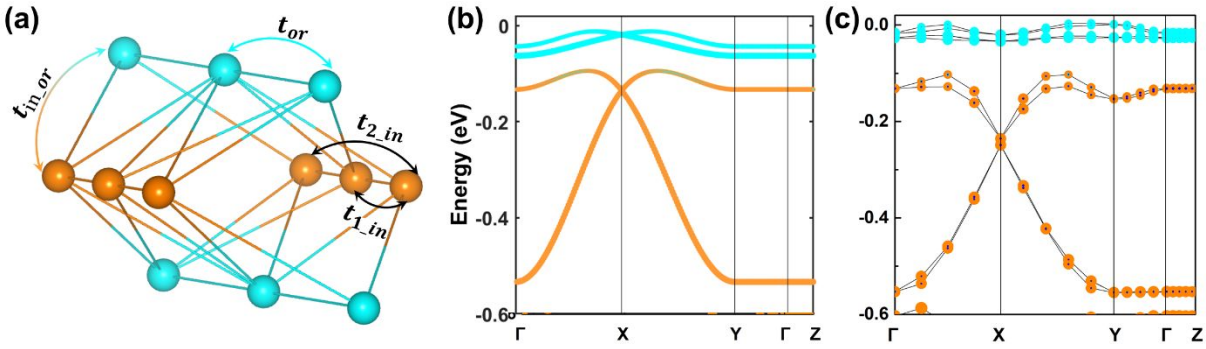

Figure 7. (**a**) Illustration of orbital hopping in a lattice model for the (Cy7)PbI3·2DMF perovskite. The nearest and next-nearest hopping integrals between $[PbI_3]$ octahedra are indicated by parameters t_{1_in} and t_{2_in}; the nearest hopping between Cy7, by t_{or}; and the nearest hopping between Cy7 and $[PbI_3]$, by t_{in_or}. (**b**) Band structures fitted by a TB model with the parameters ε_{or} = – 0.05 eV, ε_{in} = – 0.22 eV, t_{1_in}=0.105 eV, t_{2_in}=0.05 eV, t_{or}=0.008 eV, t_{in_or}=0.039 eV. (**c**) DFT-HSE-SOC band structure of (Cy7)PbI_3·2DMF, which is used as a reference for the model presented in (**b**). The cyan and orange colors represent the contributions from the organic and inorganic components, respectively.

We further note that, as hybridization occurs between the Cy7 LUMO+1 level and the CBM of the perovskite, if a higher energy excitation (at about 3.6 eV, to be compared with the HOMO-LUMO gap of ~ 1.7 eV for Cy7) can be absorbed by the perovskite chains, DET could appear between the chains and the Cy7 molecules. However, under these conditions, Forster energy transfer (FRET) could become the dominant energy transfer mechanism and compete with the DET. As such, the energy transfer mechanisms in these systems are expected to be complex and should be evaluated by calculating various parameters such as the transition dipole-dipole interactions and electronic couplings. We leave this discussion to future work on systems where strong wavefunction delocalization between the organic and inorganic components can be realized.

IV. Frontier molecular orbitals and excited-state properties in the HOIP cluster models

To confirm the validity of the selected cluster model for the Cy7-perovskite (**Figure 8a,** which corresponds to a $(Cy7)_{12}Pb_6I_{24}$ stoichiometry and has a total dipole moment of 0.01 Debye) and of the model for the VBB-perovskite **(Figure S3**, which corresponds to a $(VBB)_{12}Pb_6I_{24}$ stoichiometry and has a total dipole moment of 76.7 Debye), we first calculated their HOMO-LUMO gaps in the ground state using the same functional as the one adopted in the periodic-structure calculations, *i.e.*, the HSE06 functional[51] with 35% Hartree-Fock exchange. The calculated HOMO-LUMO gaps for the Cy7-perovskite and VBB-perovskite clusters are 1.63 and 2.12 eV, respectively. These values are in very good agreement with those calculated for the periodic-structure systems at the HSE+SOC level of theory (1.66 eV and 2.01 eV, respectively). However, we note that the ground-state wavefunctions and excited-state natural transition orbitals cannot be well characterized in the VBB-perovskite cluster. This can be attributed to the presence of the large 76.7 Debye dipole moment, which we were not able to reduce; indeed, unlike the

situation in the Cy7-cluster, where the intrinsic molecular dipole aligns with the molecular chain axis and can be made to nearly vanish given the intermolecular packing in the selected cluster, the molecular dipoles in the VBB cluster are aligned along the in-plane direction and cannot be canceled given that the molecules stack along the direction nearly perpendicular to the plane. The VBB-perovskite cluster was therefore not considered in the following discussion. Also, we note that DMF molecules have not been explicitly incorporated in the cluster models since they have no significant contributions to the conduction band and valence band edge states, as illustrated by the calculated projected densities of states for the periodic structures (see **Figure 3**).

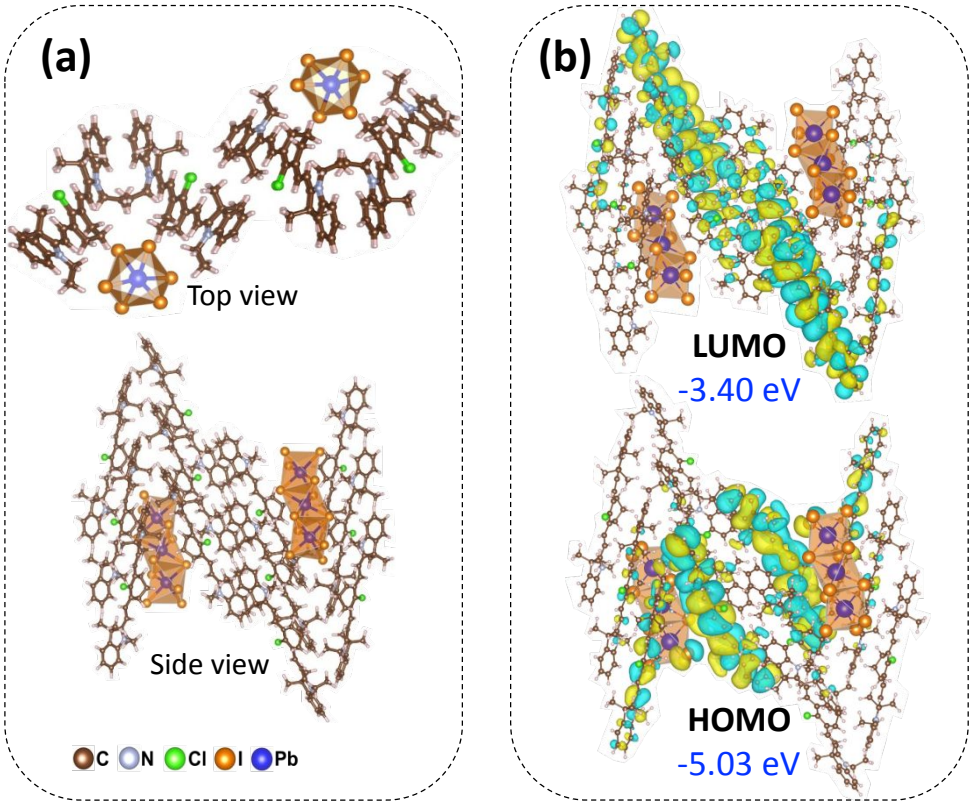

Figure 8. (**a**) Illustrations of the $(Cy7)_{12}Pb_6I_{24}$ cluster model: top view and side view. (**b**) Frontier molecular orbitals of the $(Cy7)_{12}Pb_6I_{24}$ cluster calculated at the HSE06 level. Isodensity surfaces with a contour of ±0.004 a.u. have been used to represent positive (yellow) and negative (green) phases of the wavefunction.

The HSE06-calculated HOMO and LUMO wavefunctions of the $(Cy7)_{12}Pb_6I_{24}$ cluster are illustrated in **Figure 8b**. Significant electronic coupling between the $[PbI_3]^-$ octahedra and the Cy7 cations can be observed at the HOMO level but not at the LUMO level. This situation remains the same for the three levels nearly degenerate with the HOMO and the level nearly degenerate with the LUMO, see **Figure S4**. Overall, these features are consistent with the partial charge density distributions obtained in the periodic-structure calculations.

To provide an accurate description of the molecular (cluster) excited states, we carried out TDDFT calculations at the long-range corrected ωB97X-D level. **Figure 9** displays the natural transition orbitals for holes and electrons in the lowest singlet excited states that have a non-zero oscillator strength and absorb in the energy range from 1.8 to 2.1 eV. In the lowest three such singlet energy states S_1, S_4, and S_5 (at ~1.8 eV, see **Table S2** in the SI) and the somewhat higher S_{12} state (at 2.1 eV), weak hybridization between the $[PbI_3]^-$ fragments and the organic cations can be observed for the hole states; the S_{12} state corresponds to the excitation with the highest oscillator strength as it is mainly associated with contributions from closely packed Cy7 molecules. In contrast, the absorbing S_8 and S_{10} states represent excitations localized on the Cy7 molecules only.

These results indicate that the low-lying excited singlet states consist of, on the one hand, hybridized holes and, on the other hand, electrons localized on the organic spacers, a feature that points to the emergence of a charge transfer (CT) component. Therefore, we analyzed the CT contributions from the inorganic to the organic fragment for all low-lying excited states with non-zero transition oscillator strength. These contributions turn out to be only about 1.3% at the most (see **Table S2** in the SI). While such a small CT contribution cannot induce a well-defined CT peak in the absorption spectrum, it can lead to some absorption band broadening. Overall, the

cluster results confirm the expectations coming from the periodic boundary calculations, *i.e.*, that there exists only a weak hybridization between the molecular HOMO level and the top valence electronic states of the perovskite in the (Cy7)PbI_3 system.

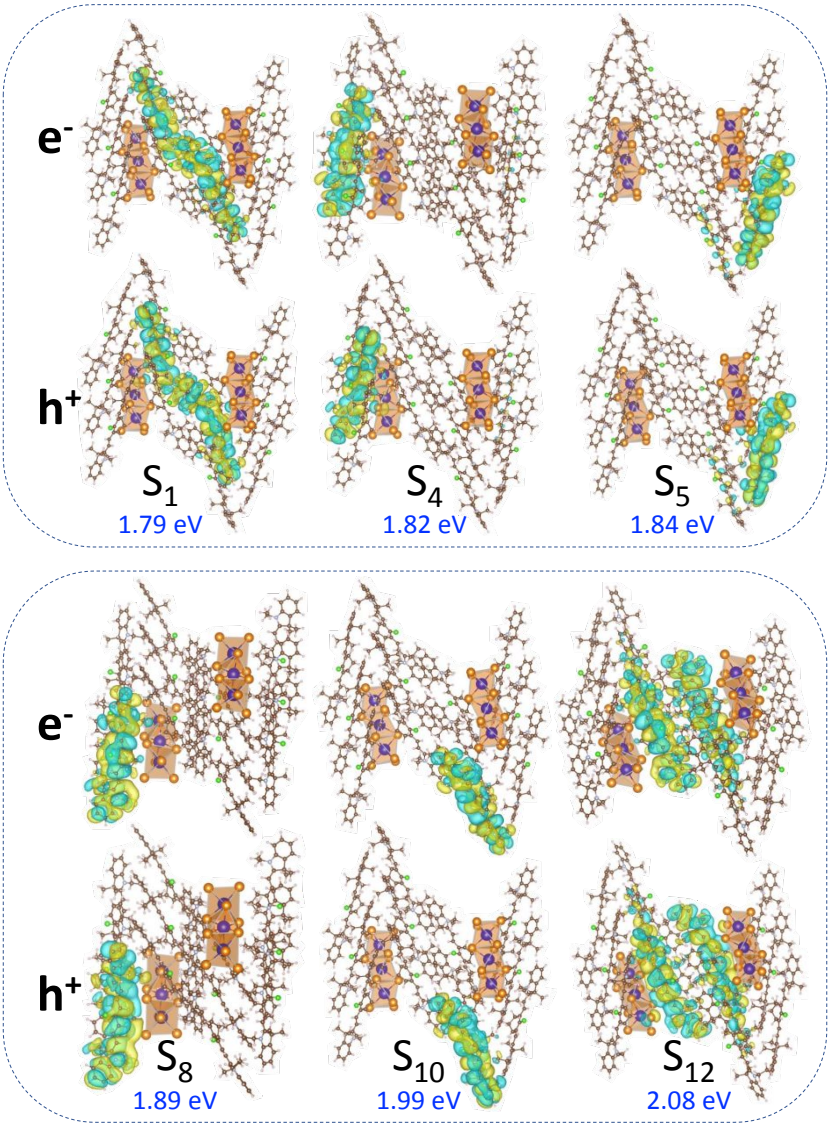

Figure 9. Natural transition orbitals for holes and electrons in the low-lying singlet excited states absorbing in the energy range from 1.8 (top) to 2.1 eV (bottom), as obtained for the $(Cy7)_{12}Pb_6I_{24}$ cluster calculated at the ωB97X-D level. The symbols e^- and h^+ stand for electron and hole, respectively. Isodensity surfaces with a contour of ±0.004 a.u. have been used to represent the positive (yellow) and negative (green) phases of the wavefunctions.

To further quantify the impact of the weak wavefunction delocalization on the optical absorption, we simulated the absorption spectra of the $(Cy7)_{12}Pb_6I_{24}$ cluster and the iodide salt of the cyanine chromophore (Cy7-I), with DMF considered as an implicit solvent, see **Figure 10.** The absorption peaks of Cy7-I and the $(Cy7)_{12}Pb_6I_{24}$ cluster are centered at 573 nm (2.16 eV) and 597 nm (2.08 eV), respectively, which corresponds to a red-shift of 0.08 eV in the hybrid perovskite. A broadening in the spectrum of $(Cy7)_{12}Pb_6I_{24}$ (full width at half-maximum (fwhm) ~ 3300 cm^{-1}, 0.41 eV) in comparison to that for Cy-I (fwhm ~ 3000 cm^{-1}, 0.37 eV) is observed on the low-energy side; this can be attributed to the lowest hybrid-type excitations (S_1, S_4, and S_5) induced by the electronic couplings between the organic and inorganic components at the valence band edges. These results are in qualitative agreement with the features observed in the experimental absorption spectra, where the Cy7-I crystal presents a sharp peak centered at 766 nm, while a significant broadening of 180 nm (from 820 to 1000 nm, ~ 0.27 eV) with a slightly red-shifted peak has been reported for the $Cy7PbI_3.2DMF$ crystal.[36,76]

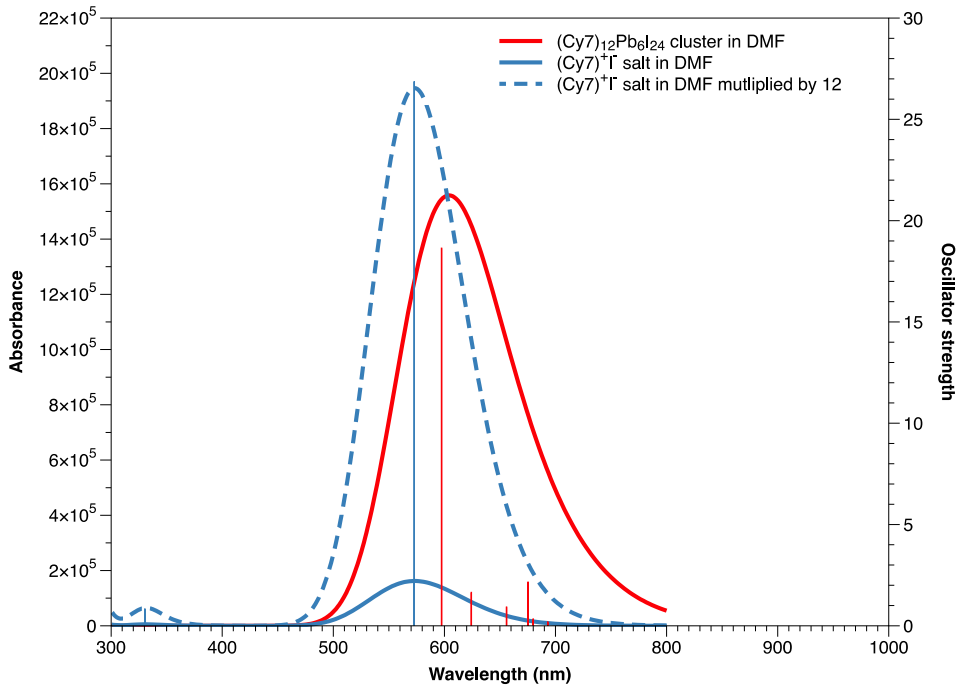

Figure 10. Absorption spectra of the $(Cy7)_{12}Pb_6I_{24}$ cluster (red line), Cy7-I (blue solid line), and Cy7-I scaled to 12 molecules (blue dashed line), as calculated with time-dependent DFT at the ωB97X-D level and implicit consideration of DMF as solvent.

Conclusions

We have investigated the electronic and optical properties of two dye cation-based 1D hybrid perovskites at the DFT and TDDFT levels, $(Cy7)PbI_3$ and $(VBB)PbI_3$. While both systems display a close alignment of the top valence band associated with the perovskite chains and the highest occupied molecular orbitals of the dye cations, an electronic coupling between the organic and inorganic components has been calculated only in the case of the cyanine-based perovskite, for which there then occurs wavefunction delocalization in the top valence bands. Using tight-binding model analyses, the electronic coupling strength between the Cy7 HOMO level and the PbI_3 chains is estimated to be ~39 meV, which is comparable with the value evaluated for the $AnBEPbI_4$ 2D perovskite. The role of this electronic coupling in the excited-state properties has been further

described by the observation of organic-inorganic hybridization in the hole states and the minor charge-transfer characteristics of the low-lying singlet excitations. Such a hybridization then contributes to a small broadening and red-shift of the lowest optical absorption band in a $(Cy7)_{12}Pb_6I_{24}$ cluster with respect to the Cy7-I salt.

Our detailed characterization of the electronic coupling between the organic and inorganic components in a 1D perovskite underlines that there exists a large set of parameters that can be tuned to manipulate the electronic and optical properties of hybrid perovskite materials. While the systems investigated here present only minor wavefunction-delocalization and charge-transfer characteristics, we anticipate that further tuning of the organic spacers, the hybrid perovskite structures, and the metal and halogen atoms can lead to the design of hybrid perovskites with stronger electronic couplings and novel hybrid-exciton behaviors.

Acknowledgements

This work was supported by the Office of Naval Research under Award No. N00014-22-1-2379 and by the College of Science of the University of Arizona. The computing resources were provided by the Research Data Center at the University of Arizona.

References

1 I. C. Smith, E. T. Hoke, D. Solis-Ibarra, M. D. McGehee and H. I. Karunadasa, *Angewandte Chemie*, 2014, **126**, 11414–11417.

2 D. H. Cao, C. C. Stoumpos, O. K. Farha, J. T. Hupp and M. G. Kanatzidis, *J Am Chem Soc*, 2015, **137**, 7843–7850.

3 H. Tsai, W. Nie, J. C. Blancon, C. C. Stoumpos, R. Asadpour, B. Harutyunyan, A. J. Neukirch, R. Verduzco, J. J. Crochet, S. Tretiak, L. Pedesseau, J. Even, M. A. Alam, G. Gupta, J. Lou, P. M. Ajayan, M. J. Bedzyk, M. G. Kanatzidis and A. D. Mohite, *Nature*, 2016, **536**, 312–316.

4 L. Mao, C. C. Stoumpos and M. G. Kanatzidis, *J Am Chem Soc*, 2019, **141**, 1171–1190.

5 F. Zhang, H. Lu, J. Tong, J. J. Berry, M. C. Beard and K. Zhu, *Energy Environ Sci*, 2020, **13**, 1154–1186.

6 M. Era, K. Maeda and T. Tsutsui, *Chem Phys Lett*, 1998, **296**, 417–420.

7 D. B. Mitzi, K. Chondroudis and C. R. Kagan, *Inorg Chem*, 1999, **38**, 6246–6256.

8 M. Braun, W. Tuffentsammer, H. Wachtel and H. C. Wolf, *Chem Phys Lett*, 1999, **307**, 373–378.

9 K. Ema, M. Inomata, Y. Kato, H. Kunugita and M. Era, *Phys Rev Lett*, 2008, **100**, 257401.

10 B. Saparov and D. B. Mitzi, *Chem Rev*, 2016, **116**, 4558–4596.

11 J. Byun, H. Cho, C. Wolf, M. Jang, A. Sadhanala, R. H. Friend, H. Yang, T.-W. Lee, J. Byun, H. Cho, C. Wolf, T.-W. Lee, M. Jang, H. Yang, A. Sadhanala and R. H. Friend, *Adv Mater*, 2016, **28**, 7515–7520.

12 N. Wang, L. Cheng, R. Ge, S. Zhang, Y. Miao, W. Zou, C. Yi, Y. Sun, Y. Cao, R. Yang, Y. Wei, Q. Guo, Y. Ke, M. Yu, Y. Jin, Y. Liu, Q. Ding, D. Di, L. Yang, G. Xing, H. Tian, C. Jin, F. Gao, R. H. Friend, J. Wang and W. Huang, *Nat Photonics*, 2016, **10**, 699–704.

13 Y. Liu, H. Ye, Y. Zhang, K. Zhao, Z. Yang, Y. Yuan, H. Wu, G. Zhao, Z. Yang, J. Tang, Z. Xu and S. (Frank) Liu, *Matter*, 2019, **1**, 465–480.

14 C. Sun, Y. Jiang, M. Cui, L. Qiao, J. Wei, Y. Huang, L. Zhang, T. He, S. Li, H. Y. Hsu, C. Qin, R. Long and M. Yuan, *Nat Commun*, 2021, **12**, 1–11.

15 E. R. Dohner, E. T. Hoke and H. I. Karunadasa, *J Am Chem Soc*, 2014, **136**, 1718–1721.

16 M. D. Smith and H. I. Karunadasa, *Acc Chem Res*, 2018, **51**, 619–627.

17 Z. Yuan, C. Zhou, Y. Tian, Y. Shu, J. Messier, J. C. Wang, L. J. van de Burgt, K. Kountouriotis, Y. Xin, E. Holt, K. Schanze, R. Clark, T. Siegrist and B. Ma, *Nat Commun*, 2017, **8**, 1–7.

18 D. Cortecchia, J. Yin, A. Petrozza and C. Soci, *J Mater Chem C*, 2019, **7**, 4956–4969.

19 Y. Wang, S. Guo, H. Luo, C. Zhou, H. Lin, X. Ma, Q. Hu, M. H. Du, B. Ma, W. Yang and X. Lü, *J Am Chem Soc*, 2020, **142**, 16001–16006.

20 Z. Qi, H. Gao, X. Yang, Y. Chen, F. Q. Zhang, M. Qu, S. L. Li and X. M. Zhang, *Inorg Chem*, 2021, **60**, 15136–15140.

21 M. Era, S. Morimoto, T. Tsutsui and S. Saito, *Appl Phys Lett*, 1994, **65**, 678.

22 A. Akriti, E. Shi and L. Dou, *Trends Chem*, 2019, **1**, 365–367.

23 B. R. Sutherland and E. H. Sargent, *Nat Photonics*, 2016, **10**, 295–302.

24 H. Zhang, Q. Liao, Y. Wu, Z. Zhang, Q. Gao, P. Liu, M. Li, J. Yao, H. Fu, H. Zhang, Y. Wu, J. Yao, H. Fu, Q. Liao, Z. Zhang, Q. Gao, P. Liu and M. Li, *Adv Mater*, 2018, **30**, 1706186.

25 C. M. Raghavan, T. P. Chen, S. S. Li, W. L. Chen, C. Y. Lo, Y. M. Liao, G. Haider, C. C. Lin, C. C. Chen, R. Sankar, Y. M. Chang, F. C. Chou and C. W. Chen, *Nano Lett*, 2018, **18**, 3221–3228.

26 C. Qin, A. S. D. Sandanayaka, C. Zhao, T. Matsushima, D. Zhang, T. Fujihara and C. Adachi, *Nature*, 2020, **585**, 53–57.

27 V. M. Goldschmidt, *Naturwissenschaften*, 1926, **14**, 477–485.

28 V. M. Goldschmidt, *T Faraday Soc*, 1929, **25**, 253–283.

29 C. Liu, W. Huhn, K. Z. Du, A. Vazquez-Mayagoitia, D. Dirkes, W. You, Y. Kanai, D. B. Mitzi and V. Blum, *Phys Rev Lett*, 2018, **121**, 146401.

30 W. A. Dunlap-Shohl, E. T. Barraza, A. Barrette, S. Dovletgeldi, G. Findik, D. J. Dirkes, C. Liu, M. K. Jana, V. Blum, W. You, K. Gundogdu, A. D. Stiff-Roberts and D. B. Mitzi, *Mater Horiz*, 2019, **6**, 1707–1716.

31 Y. Gao, E. Shi, S. Deng, S. B. Shiring, J. M. Snaider, C. Liang, B. Yuan, R. Song, S. M. Janke, A. Liebman-Peláez, P. Yoo, M. Zeller, B. W. Boudouris, P. Liao, C. Zhu, V. Blum, Y. Yu, B. M. Savoie, L. Huang and L. Dou, *Nat Chem*, 2019, **11**, 1151–1157.

32 Z. Huang, B. P. Bloom, X. Ni, Z. N. Georgieva, M. Marciesky, E. Vetter, F. Liu, D. H. Waldeck and D. Sun, *ACS Nano*, 2020, **14**, 10370–10375.

33 Q. Dai, H. Li, G. Sini, J.-L. Bredas, Q. Dai, H. Li, J.-L. Bredas and G. Sini, *Adv Funct Mater*, 2022, **32**, 2108662.

34 J. Xue, R. Wang, X. Chen, C. Yao, X. Jin, K. L. Wang, W. Huang, T. Huang, Y. Zhao, Y. Zhai, D. Meng, S. Tan, R. Liu, Z. K. Wang, C. Zhu, K. Zhu, M. C. Beard, Y. Yan and Y. Yang, *Science*, 2021, **371**, 636–640.

35 H. Hu, D. Zhao, Y. Gao, X. Qiao, T. Salim, B. Chen, E. E. M. Chia, A. C. Grimsdale and Y. M. Lam, *Chem Mater*, 2019, **31**, 2597–2602.

36 A. C. Véron, A. Linden, N. A. Leclaire, E. Roedern, S. Hu, W. Ren, D. Rentsch and F. A. Nüesch, *J Phys Chem Lett*, 2018, **9**, 2438–2442.

37 A. Starkholm, L. Kloo and P. H. Svensson, *J Am Chem Soc*, 2020, **142**, 18437–18448.

38 Y. Lin, R. Weissleder and C. H. Tung, *Bioconjug Chem*, 2002, **13**, 605–610.

39 F. Song, X. Peng, E. Lu, R. Zhang, X. Chen and B. Song, *J Photoch Photobio A*, 2004, **168**, 53–57.

40 X. Peng, F. Song, E. Lu, Y. Wang, W. Zhou, J. Fan and Y. Gao, *J Am Chem Soc*, 2005, **127**, 4170–4171.

41 A. Samanta, M. Vendrell, R. Das and Y. T. Chang, *Chem Commun*, 2010, **46**, 7406–7408.

42 H. A. Shindy, *Dyes Pigments*, 2017, **145**, 505–513.

43 L. Feng, W. Chen, X. Ma, S. H. Liu and J. Yin, *Org Biomol Chem*, 2020, **18**, 9385–9397.

44 L. Strekowski, M. Lipowska and G. Patonay, *J Org Chem*, 1992, **57**, 4578–4580.

45 Z. Zhang and S. Achilefu, *Org Lett*, 2004, **6**, 2067–2070.

46 S. Liu, H. Luo, N. Li, Z. Liu and W. Zheng, *Anal Chem*, 2001, **73**, 3907–3914.

47 L. Kong and S. Liu, *Int J Environ An Ch*, 2013, **93**, 23–34.

48 T. Gessner and U. Mayer, in *Ullmann's Encyclopedia of Industrial Chemistry*, John Wiley & Sons, Ltd, 2000.

49 G. Kresse and J. Furthmüller, *Phys Rev B*, 1996, **54**, 11169.

50 J. P. Perdew, K. Burke and M. Ernzerhof, *Phys Rev Lett*, 1997, **78**, 1396.

51 J. Heyd, G. E. Scuseria and M. Ernzerhof, *J Chem Phys*, 2003, **118**, 8207.

52 A. v. Krukau, O. A. Vydrov, A. F. Izmaylov and G. E. Scuseria, *J Chem Phys*, 2006, **125**, 224106.

53 S. Grimme, J. Antony, S. Ehrlich and H. Krieg, *J Chem Phys*, 2010, **132**, 154104.

54 V. Wang, N. Xu, J. C. Liu, G. Tang and W. T. Geng, *Comput Phys Commun*, 2021, **267**, 108033.

55 I. H. Nayyar, E. R. Batista, S. Tretiak, A. Saxena, D. L. Smith and R. L. Martin, *J Phys Chem Lett*, 2011, **2**, 566–571.

56 I. H. Nayyar, E. R. Batista, S. Tretiak, A. Saxena, D. L. Smith and R. L. Martin, *J Polym Sci Pol Phys*, 2013, **51**, 935–942.

57 M. L. Steigerwald and L. E. Brus, *Acc Chem Res*, 1990, **23**, 183–188.

58 V. N. Soloviev, A. Eichhöfer, D. Fenske and U. Banin, *J Am Chem Soc*, 2000, **122**, 2673–2674.

59 A. Kasuya, R. Sivamohan, Y. A. Barnakov, I. M. Dmitruk, T. Nirasawa, V. R. Romanyuk, V. Kumar, S. v. Mamykin, K. Tohji, B. Jeyadevan, K. Shinoda, T. Kudo, O. Terasaki, Z. Liu, R. v. Belosludov, V. Sundararajan and Y. Kawazoe, *Nat Mater*, 2004, **3**, 99–102.

60 H. J. Zhai, X. Huang, L. F. Cui, X. Li, J. Li and L. S. Wang, *J Phys Chem A*, 2005, **109**, 6019–6030.

61 R. R. Chandler, S. R. Bigham and J. L. Coffer, *J Chem Educ*, 1993, **70**, A7.

62 Z. Gao, Y. Bai, M. Wang, G. Mao, X. Liu, P. Gao, W. Yang, X. Ding and J. Yao, *J Phys Chem C*, 2022, **126**, 13409–13415.

63 Y. Chen, X. Ding, L. Yang, Y. Wang, J. I. Gurti, M. Wang, W. Li, X. Wang and W. Yang, *Phys Chem Chem Phys*, 2022, **24**, 14375–14389.

64 Z. Gao, S. Chen, Y. Bai, M. Wang, X. Liu, W. Yang, W. Li, X. Ding and J. Yao, *Phys Chem Chem Phys*, 2021, **23**, 11548–11556.

65 G. Giorgi, T. Yoshihara and K. Yamashita, *Phys Chem Chem Phys*, 2016, **18**, 27124–27132.

66 H. Fang and P. Jena, *J Phys Chem Lett*, 2016, **7**, 1596–1603.

67 A. J. Neukirch, W. Nie, J. C. Blancon, K. Appavoo, H. Tsai, M. Y. Sfeir, C. Katan, L. Pedesseau, J. Even, J. J. Crochet, G. Gupta, A. D. Mohite and S. Tretiak, *Nano Lett*, 2016, **16**, 3809–3816.

68 J. Yin, H. Li, D. Cortecchia, C. Soci and J. L. Brédas, *ACS Energy Lett*, 2017, **2**, 417–423.

69 M. J. Frisch, G. W. Trucks, H. B. Schlegel, G. E. Scuseria, M. A. Robb, J. R. Cheeseman, G. Scalmani, V. Barone, G. A. Petersson, H. Nakatsuji, X. Li, M. Caricato, A. v. Marenich, J. Bloino, B. G. Janesko, R. Gomperts, B. Mennucci, H. P. Hratchian, J. v. Ortiz, A. F. Izmaylov, J. L. Sonnenberg, D. Williams-Young, F. Ding, F. Lipparini, F. Egidi, J. Goings, B. Peng, A. Petrone, T. Henderson, D. Ranasinghe, V. G. Zakrzewski, J. Gao, N. Rega, G. Zheng, W. Liang, M. Hada, M. Ehara, K. Toyota, R. Fukuda, J. Hasegawa, M. Ishida, T. Nakajima, Y. Honda, O. Kitao, H. Nakai, T. Vreven, K. Throssell, J. A. , Jr. Montgomery, J. E. Peralta, F. Ogliaro, M. J. Bearpark, J. J. Heyd, E. N. Brothers, K. N. Kudin, V. N. Staroverov, T. A. Keith, R. Kobayashi, J. Normand, K. Raghavachari, A. P. Rendell, J. C. Burant, S. S. Iyengar, J. Tomasi, M. Cossi, J. M. Millam, M. Klene, C. Adamo, R. Cammi, J. W. Ochterski, R. L. Martin, K. Morokuma, O. Farkas, J. B. Foresman and D. J. Fox, 2017.

70 J. da Chai and M. Head-Gordon, *Phys Chem Chem Phys*, 2008, **10**, 6615–6620.

71 R. Ditchfield, W. J. Hehre and J. A. Pople, *J Chem Phys*, 2003, **54**, 724.

72 A. Schäfer, H. Horn and R. Ahlrichs, *J Chem Phys*, 1992, **97**, 2571.

73 Y. Takano and K. N. Houk, *J Chem Theory Comput*, 2005, **1**, 70–77.

74 R. L. Martin, *J Chem Phys*, 2003, **118**, 4775.

75 T. Lu and F. Chen, *J Comput Chem*, 2012, **33**, 580–592.

76 A. C. Véron, University of Zürich, 2017.